

Unsupervised MRI Reconstruction via Zero-Shot Learned Adversarial Transformers

Yilmaz Korkmaz, Salman UH Dar, Mahmut Yurt, Muzaffer Özbey, and Tolga Çukur

Abstract—Supervised deep learning has swiftly become a workhorse for accelerated MRI in recent years, offering state-of-the-art performance in image reconstruction from undersampled acquisitions. Training deep supervised models requires large datasets of undersampled and fully-sampled acquisitions typically from a matching set of subjects. Given scarce access to large medical datasets, this limitation has sparked interest in unsupervised methods that reduce reliance on fully-sampled ground-truth data. A common framework is based on the deep image prior, where network-driven regularization is enforced directly during inference on undersampled acquisitions. Yet, canonical convolutional architectures are suboptimal in capturing long-range relationships, and randomly initialized networks may hamper convergence. To address these limitations, here we introduce a novel unsupervised MRI reconstruction method based on zero-Shot Learned Adversarial TransformerERs (SLATER). SLATER embodies a deep adversarial network with cross-attention transformer blocks to map noise and latent variables onto MR images. This unconditional network learns a high-quality MRI prior in a self-supervised encoding task. A zero-shot reconstruction is performed on undersampled test data, where inference is performed by optimizing network parameters, latent and noise variables to ensure maximal consistency to multi-coil MRI data. Comprehensive experiments on brain MRI datasets clearly demonstrate the superior performance of SLATER against state-of-the-art unsupervised methods.

Index Terms—Unsupervised learning, MRI, reconstruction, adversarial, transformers, zero shot, generative.

I. INTRODUCTION

MAGNETIC Resonance Imaging (MRI) is a clinical powerhouse in diagnostic imaging due to its excellent soft tissue contrast and noninvasiveness. Yet, low spin polarization at mainstream field strengths limits signal-to-noise ratio and necessitates prolonged exams. Extensive MRI exams incur added economic costs and lower use efficiency, and they may not be possible in uncooperative patient populations. A dire consequence is administration of MRI exams that are in lower quality and/or diversity, which projects poorly onto

This study was supported in part by a TUBA GEBIP 2015 fellowship, and a BAGEP 2017 fellowship (Corresponding author: Tolga Çukur).

Y. Korkmaz, S. UH. Dar, M. Yurt, and M. Özbey are with the Department of Electrical and Electronics Engineering, Bilkent University, Ankara, Turkey (e-mails: {korkmaz, salman, mahmut, muzaffer}@ee.bilkent.edu.tr).

T. Çukur is with the Department of Electrical and Electronics Engineering, Bilkent University, TR-06800 Ankara, Turkey, also with the National Magnetic Resonance Research Center, Bilkent University, TR-06800 Ankara, Turkey, and also with the Neuroscience Program, Sabuncu Brain Research Center, Bilkent University, TR-06800 Ankara, Turkey (e-mail: cukur@ee.bilkent.edu.tr).

diagnostic utility. Accelerated MRI techniques aim to address this fundamental problem by performing undersampled acquisitions in MRI, and then solving the inverse problem of image reconstruction from available k-space data [1]–[4].

Image reconstruction from undersampled MRI acquisitions is an ill-posed inverse problem whose solution is attempted using prior information [5], [6]. Given the performance leap that deep neural networks (DNNs) have enabled in challenging inverse problems, recent studies have quickly adopted end-to-end deep learning methods for MRI reconstruction [5], [6]. Supervised learning has rapidly become a workhorse in this area, where reconstruction models are trained on paired sets of undersampled and fully-sampled reference data. The weights of the trained model are then be fixed for inference on test samples. In recent years, successful supervised reconstruction methods have been proposed with architectures including basic convolution neural networks (CNNs) [7]–[9], residual CNNs [10], [11], multi-layer perceptrons (MLP) [12], [13], physics-guided unrolled CNN networks [14]–[22], recurrent CNNs [22]–[24], generative adversarial networks (GANs) [24]–[28], Wavelet-transform assisted CNNs [25], [29], and variational networks [30]–[33]. With their exceptional reconstruction performance, supervised DNN models are current state-of-the-art in MRI. However, it is fraud with challenges to compile large datasets of paired undersampled and fully-sampled data in many MRI applications, given the difficulties in collection and sharing of medical image data [34].

Several powerful approaches have been proposed to relax data requirements in training of MRI reconstruction models. A group of studies adopt models pretrained in a separate data-abundant domain [35], [36], or perform residual learning to map outputs of traditional parallel imaging or compressed sensing reconstructions to ground truth [37]. A second group aims to enable learning from unpaired sets of undersampled and fully-sampled data [38]–[41]. Recent studies have introduced self-supervision strategies to train models on undersampled data [42]–[52]. These unsupervised methods fix model parameters during inference on test samples, so post-training adaptation might be needed to mitigate performance loss [53], [54]. A fundamentally different approach is the deep image prior framework, where reconstructions are regularized via randomly initialized CNNs [55]–[61] that might suffer from limited sensitivity of CNN models in capturing long-range dependencies and suboptimal convergence due to random priors [62].

Here, we introduce a novel unsupervised MRI reconstruction method based on zero-shot learned adversarial trans-

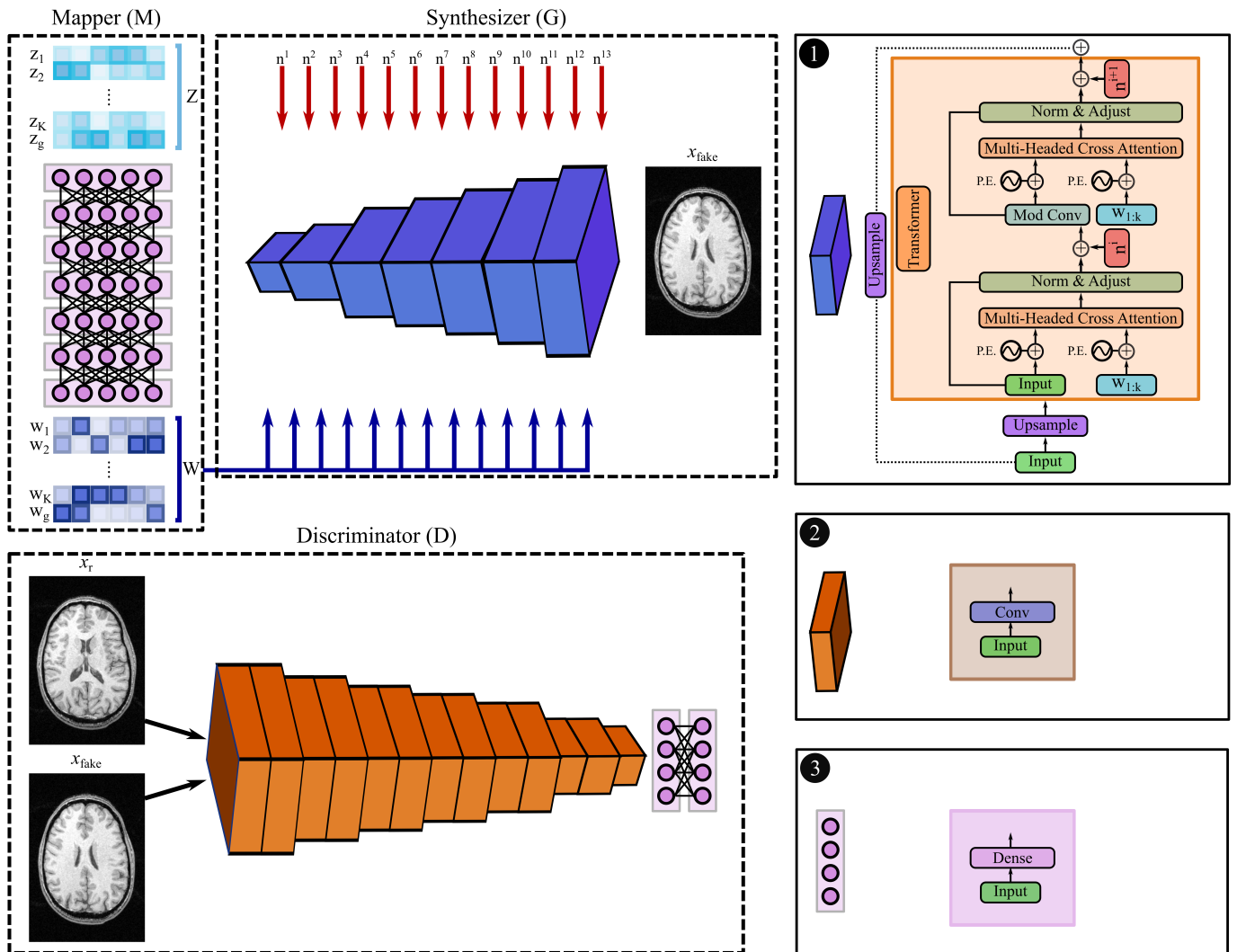


Fig. 1: SLATER is based on an unconditional adversarial architecture with a mapper (M), a synthesizer (G), and a discriminator (D). M projects raw latent variables (Z) onto K local (w_1, \dots, w_K) variables and one global (w_g) latent variable. G is a multi-layer architecture where image resolution is progressively increased across layers. Within intermediate layers, a convolutional upsampling block is followed by a cross-attention transformer block (see 1). The transformer block receives global and local latent variables, noise variables and positional encoding (P.E.) for latents and image features. D enables adversarial learning while it receives as input synthetic and real MR images. It is composed of convolutional and dense blocks (see 2, 3). Unsupervised training is performed on the SLATER model in a self-encoding task to capture high-quality MRI priors.

formers (SLATER) to enhance generalization performance and inference efficiency (Fig. 1). The proposed method expresses the reconstruction as a nonlinear mapping from an input space containing noise and latent variables onto the MR image¹. This nonlinear mapping is based on a style-generative adversarial architecture that allows improved control of image features across the network [64], [65]. To improve capture of global context and long-range dependencies, the adversarial network is composed of transformer blocks with cross-attention mechanism between latent variables and image features. Cross-attention is limited to capture interactions among a compact set of latents and features to avoid quadratic computational burden of traditional self-attention transformers [66]. To improve convergence, a zero-shot learning strategy is adopted where the

adversarial network is pretrained in a self-supervised encoding task to capture a high-quality MRI prior. During inference, network parameters, latent and noise variables are optimized to ensure maximal consistency to undersampled multi-coil MRI data (Fig. 2).

The proposed method does not require paired training datasets, or leverage fully-sampled ground truths to train reconstruction models. It performs reconstruction via reverse inference on test samples, so it enables subject-specific adaptation of the reconstruction model for improved generalization. For demonstration, we compared SLATER against (1) a fully-supervised model (GAN_{sup}) trained for specific MR contrasts and acceleration rates [28], (2) a self-supervised model (SSDU) trained for specific contrasts and acceleration rates [45], (3) a zero-shot learned GAN prior model (GAN_{prior}) [65],

¹see [63] for a preliminary version of this work presented at ISMRM 2021

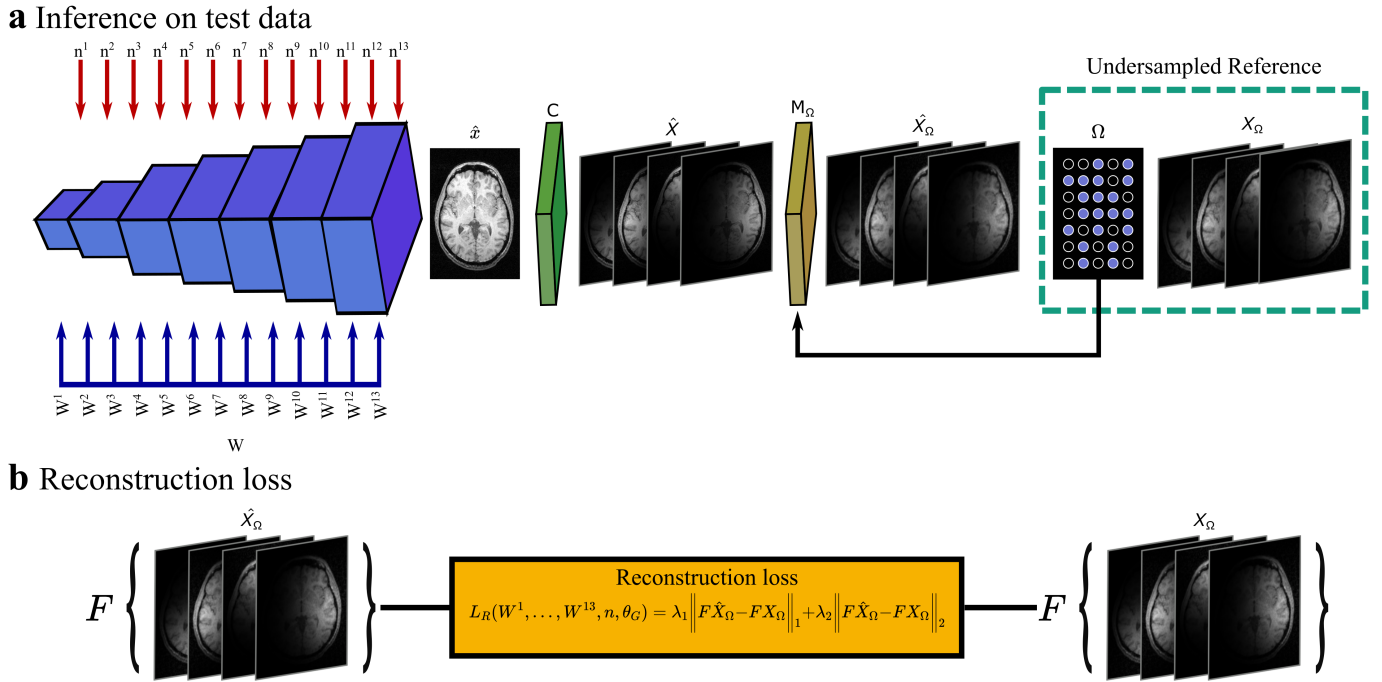


Fig. 2: (a) The generative model in SLATER is adapted to perform zero-shot reconstruction of accelerated MRI acquisitions. (b) To do this, the network prior consisting of noise (n), latent variables (W) and weights (θ_C) are optimized during inference, so as to maximize consistency between the reconstructed and undersampled data selectively over the acquired subset of k -space samples.

(4) a zero-shot learned self-attention GAN model (SAGAN) [67], (5) a DIP variant of $\text{GAN}_{\text{prior}}$ (GAN_{DIP}), (6) a DIP variant of SAGAN ($\text{SAGAN}_{\text{DIP}}$), and (7) a DIP variant of SLATER ($\text{SLATER}_{\text{DIP}}$).

Contributions:

- A novel unsupervised reconstruction technique is introduced for accelerated MRI that learns high-quality MRI priors in a self-supervised encoding task, and performs sample-specific model adaptation for inference.
- For the first time in literature, an adversarial network with cross-attention transformer blocks is introduced for MRI reconstruction, to allow incorporation of long-range dependencies without computational burden.
- Demonstrations are provided on brain MRI data to show that SLATER significantly improves reconstruction quality compared to several state-of-the-art unsupervised methods.

II. RELATED WORK

Unsupervised methods for MRI reconstruction have to rely on various forms of self-supervision while lowering reliance on fully-sampled ground truth data. Prior self-supervision strategies in MRI include use of proxy reconstruction losses based on data-consistency in undersampled k -space [42], [43], cycle-consistent models with adversarial loss only defined on undersampled data [44], k -space losses in predicting masked-out samples in undersampled acquisitions [45]–[47], image-domain losses in predicting masked-out images in multi-image data [48]–[51], or using statistical estimators for reconstruction

errors [52]. Note that these unsupervised methods fix weights of trained models during inference, so they might suffer from suboptimal generalization to test samples [53], [54].

To enhance sample-specific generalization performance, a distinct approach is based on the DIP framework [55]–[61]. DIP uses a network model to characterize the mapping from latent variables onto high-quality images [68]. In contrast to learning-based models with conditional predictions, DIP performs reverse inference on unconditional architectures. Network parameters are randomly initialized in DIP [55]–[58], although few recent studies have suggested pretraining of network weights or inputs to improve priors [59]–[61]. During inference, the network architecture then acts as a natural regularizer for the reconstruction. Despite its demonstrated power, two major limitations of DIP-based reconstruction include suboptimal capture of long-range interactions in CNN-based networks [62] and suboptimal convergence in case of random initialization.

An alternative group of methods to perform scan-specific reconstructions are inspired by traditional parallel imaging reconstructions. These methods learn local dependencies in k -space using fully-sampled auto-calibration data, and apply them broadly across k -space. Analogous to parallel imaging methods, both k -space [69]–[71], and image-domain algorithms [72] have been proposed. While these scan-specific methods alleviate the need for model training on separate data, they implicitly assume that auto-calibration data are representative of dependencies in broader k -space.

III. THEORY

In this section, we first overview the inverse problem formulation in accelerated MRI reconstructions and the deep image prior (DIP) framework as a solution to this problem. We then describe the fundamental building blocks of SLATER, including the adversarial network architecture with transformer blocks, unsupervised pretraining for capturing the MRI priors, and zero-shot learned reconstruction on test data.

A. Accelerated MRI Reconstruction

In accelerated MRI, undersampled k-space acquisitions are performed to speed up scans, typically with variable-density random sampling patterns:

$$F_u C m = y_s \quad (1)$$

where F_u is the partial Fourier operator defined by the sampling pattern, C denotes coil sensitivities, m is the target MR image and y_s are the acquired multi-coil k-space samples. For reconstruction, the target m must be computed given the available data y_s . However, the linear system in Eq.1 is underdetermined, so MRI reconstruction is an ill-posed inverse problem. To obtain high-quality reconstruction, the solution has to be regularized with additional prior information on MR images:

$$\hat{m} = \underset{m}{\operatorname{argmin}} \|y_s - F_u C m\|_2^2 + H(m) \quad (2)$$

where \hat{m} is the reconstructed image, and $H(m)$ is the regularization term. The regularization term can be designed based on sparsity priors [3] or network priors [8].

B. Deep Image Prior

The DIP framework has recently been introduced for unsupervised learning in computer vision tasks, including super resolution, inpainting and denoising [68]. The motivation of DIP is that the hierarchy of local filtering operations in CNNs constrain the set of images that can be generated, so untrained CNNs can serve as native image regularizer. DIP typically performs random initialization of network inputs and weights without any pretraining. During inference, network parameters are optimized by enforcing consistency with the available corrupted image. Thus, DIP projects the corrupted image onto the space of CNN-generatable images to filter out corruptions such as blur or noise.

The DIP method can be adopted for the MRI reconstruction problem as follows:

$$\theta^* = \underset{\theta}{\operatorname{argmin}} \|F_u C d_\theta(z) - y_s\|_1 \quad (3)$$

where θ are network weights, z are latent variables, $d_\theta(z)$ is the network mapping from latents onto the reconstructed image [55]–[59]. Both network weights and latents are randomly initialized, and the optimization in Eq.3 is performed over θ , while z is fixed. In contrast to mainstream learning-based methods, DIP inverts a random network prior to identify weights that are most consistent with the corrupted image. The reconstruction can then be expressed as:

$$\hat{m} = d_{\theta^*}(z) \quad (4)$$

Despite its prowess in MRI reconstruction tasks, DIP is traditionally based on CNN architectures, where local kernels introduce suboptimal sensitivity in capture of long-range spatial interactions. In addition, random initialization of network parameters might lead to poor convergence [73], [74].

C. Zero-shot Learned Adversarial Transformers (SLATER)

Here we introduce a novel unsupervised method for accelerated MRI that uses a deep generative model to map noise and latent variables onto MR images. Inspired by the DIP framework, SLATER performs model inversion to infer values of noise and latent variables as well as network weights that are most consistent with the undersampled measurements. Unlike prior methods, however, the nonlinear mapping is based on a style-generative adversarial network with transformer blocks having compact support and soft-attention mechanisms. A zero-shot learning strategy is proposed where latent representations are pretrained in a self-supervised encoding task. Fundamental components of SLATER are detailed in the following subsections.

Adversarial Transformer Model: The proposed technique is based on an unconditional adversarial network that receives noise and latent inputs to generate MR images [63]. Here we adopt a style-generative architecture given the success of this model family in computer vision tasks [65]. We further propose to build the network layers with cross-attention transformer blocks as inspired by a recent study on natural image synthesis [66]. These cross-attention transformers improve information flow from latent inputs to intermediate image features across the network to allow enhanced capture of long-range context. The model contains three sub-networks as depicted in Fig.1: a synthesizer that generates high-quality MR images; a mapper that prepares the set of latent variables input to the synthesizer; and a discriminator to capture MR image statistics.

1) Synthesizer (G): The synthesizer is a multi-layer architecture where each layer comprises a convolutional upsampling block to progressively increase image resolution followed by a cross-attention transformer block. Unlike conventional GANs with latents provided only at the input layer, a global ($w_g \in \mathbb{R}^{L_s}$) and K local ($W_l \in \mathbb{R}^{K \times L_s}$) intermediate latent variables are input to the synthesizer at each layer, along with sinusoidal position encoding variables. Global latents increase control over high-level features via modulation of feature maps, whereas local latents control low-level features. The cross-attention transformer blocks contain a serial cascade of sub-blocks: (cross-attention, noise injection, style-modulated convolution, cross-attention, noise injection). In contrast to vanilla transformers, alterations for image domain include noise injection for control of fine details, replacement of the fully-connected sub-block with a convolutional block for efficiency, and a repeated attention block. Each sub-block is explained in detail below.

a) Cross-Attention: The cross-attention block controls information flow from K aggregated latent components W_l to feature maps X^i . Let $X^{i-1} \in \mathbb{R}^{m \times h \times u}$ be the input of the i th

cross-attention block and $X_{vec}^{i-1} \in \mathbb{R}^{(m \times h) \times u}$ be its vectorized form. Attention maps $att_i \in \mathbb{R}^{(m \times h) \times u}$ for information flow from W_l to X_{vec}^{i-1} can be obtained as follows:

$$att_G^i = softmax \left(\frac{q_G^i(X_{vec}^{i-1})k_G^i(W_l)^T}{\sqrt{u}} \right) v_G^i(W_l) \quad (5)$$

where $q_G^i(\cdot) \in \mathbb{R}^{(m \times h) \times u}$, $k_G^i(\cdot) \in \mathbb{R}^{K \times u}$, and $v_G^i(\cdot) \in \mathbb{R}^{K \times u}$ are learnable linear projections of the i th cross-attention block, i.e., queries, keys, values, and each query and key receive the respective position encoding variables. Here, a single attention head was used to scale and shift X_{vec}^{i-1} with learnable linear projections of attention maps att_G^i to obtain X_{vec}^i .

$$X_{vec}^i = \gamma_i(att_G^i) \odot \left(\frac{X_{vec}^{i-1} - \mu(X_{vec}^{i-1})}{\sigma(X_{vec}^{i-1})} \right) + b_i(att_G^i) \quad (6)$$

where $\gamma_i(\cdot)$ and $b_i(\cdot)$ are scale and bias terms.

b) Noise Injection: To improve control over variability in fine details of feature maps, noise variables with standard normal distribution are injected onto globally and locally modulated feature maps from the cross-attention blocks. Given input $X^{i-1} \in \mathbb{R}^{m \times h \times u}$ to the i th noise injection block, the output can be given as

$$X^i = \begin{bmatrix} X^{i-1,1} + \alpha^{i,1} n^{i,1} \\ \vdots \\ X^{i-1,u} + \alpha^{i,u} n^{i,u} \end{bmatrix} \quad (7)$$

where $n^{i,u'} \in \mathbb{R}^{m \times h}$ corresponds to spatially varying noise added to u' th channel of i th block and $\alpha^{i,u'}$ is the corresponding learnable scalar.

c) Style Modulated Convolution: At the i th style modulated convolution block, the input feature maps are first modulated via an affine transformation $w_s^i \in \mathbb{R}^u$ of the global latent variable w_g . This can be achieved by scaling the relative convolutional kernels $\theta_G^i \in \mathbb{R}^{r \times r \times u \times v}$ along the input feature dimension:

$$\theta_G^i = \begin{bmatrix} w_s^{i,1} \theta_G^{i,1,1} & w_s^{i,1} \theta_G^{i,1,2} & \dots & w_s^{i,1} \theta_G^{i,1,v} \\ w_s^{i,2} \theta_G^{i,2,1} & w_s^{i,2} \theta_G^{i,2,2} & \dots & w_s^{i,2} \theta_G^{i,2,v} \\ \vdots & \vdots & \ddots & \vdots \\ w_s^{i,u} \theta_G^{i,u,1} & w_s^{i,u} \theta_G^{i,u,2} & \dots & w_s^{i,u} \theta_G^{i,u,v} \end{bmatrix} \quad (8)$$

where $\theta_G^{i,u',v'} \in \mathbb{R}^{r \times r}$ represents the kernel corresponding to i th block, u' th input feature map and v' th output feature map, $w_s^{i,u'}$ is a scalar variable corresponding to i th block and u' th input feature map, and $\theta_G^{i,u'}$ denotes modulated kernels. Note that this modulation alters the scale of the output feature maps by l2-norm of the kernels. This alteration can be compensated via normalized unit-norm kernels, $(\theta_G^{i,u'})$.

Therefore, the output feature maps can be computed as:

$$X^i = \begin{bmatrix} \sum_s X^{i-1,s} \otimes \theta_G^{i,s,1} \\ \vdots \\ \sum_s X^{i-1,s} \otimes \theta_G^{i,s,v} \end{bmatrix} \quad (9)$$

where $X^{i-1,s} \in \mathbb{R}^{m \times h}$ represents input feature maps to i th block and s corresponds to the feature index.

Architectural details of the synthesizer are provided in Supp. Text. During unsupervised pretraining, the parameters are learned to minimize a non-saturating logistic loss:

$$L_G(\theta_G) = -\mathbb{E}_{p(Z)} [\log(sig(D(G_{\theta_G}(M(Z)))))] \quad (10)$$

where $sig(\cdot)$ corresponds to the sigmoid function, θ_G are the network weights for the synthesizer, and $W = [W_l, w_g] \in \mathbb{R}^{(K+1) \times L_s}$.

2) Mapper (M): The mapper projects independent and identically distributed random variables ($Z = z_1, z_2, \dots, z_K, z_g; z \in \mathbb{R}^{L_s}$) onto the refined set of local and global latent variables ($W = w_1, w_2, \dots, w_K, w_g; w \in \mathbb{R}^{L_s}$) expected by the synthesizer. This projection has been reported to improve disentanglement of the latent space and thereby contribute to model invertability [65], [75]. M is a multi-layered architecture where each layer contains a self-attention block followed two fully-connected dense blocks. Attention blocks only process local latents (Z_l), where the maps for the j th block are given as:

$$att_M^j = softmax \left(\frac{q_M^j(Z_M^j)k_M^j(Z_M^j)^T}{\sqrt{q}} \right) v_M^j(Z_M^j) \quad (11)$$

where $Z_M^j \in \mathbb{R}^{(L_s \times K)}$ is the vector of intermediate activations of local latent variables (Z_l) at the j th block, and $q_M^j(\cdot)$, $k_M^j(\cdot)$ and $v_M^j(\cdot)$ are corresponding queries, keys and values respectively. The attention maps are used to scale and shift Z_M^j :

$$Z_M^{j'} = \gamma_M^j(att_M^j) \odot \left(\frac{Z_M^j - \mu(Z_M^j)}{\sigma(Z_M^j)} \right) + b_M^j(att_M^j) \quad (12)$$

where $Z_M^{j'} \in \mathbb{R}^{L_s}$ is the output of j th attention sub-block, $\gamma_M^j(\cdot)$ and $b_M^j(\cdot)$ are learned linear projections. The mapper is trained to minimize the following loss:

$$L_M(\theta_M) = -\mathbb{E}_{p(Z)} [\log(sig(D(G_{\theta_M}(M(Z)))))] \quad (13)$$

where θ_M are the parameters of the mapper. Details of the network architecture are mentioned in Supp. Text.

3) Discriminator (D): D enables adversarial learning to capture the statistics of MR images. It aims to distinguish the synthesizer output and real MR images. Details of the network architecture are mentioned in Supp. Text. The discriminator is trained with the logistic loss along with a gradient penalty term:

$$L_D(\theta_D) = -\mathbb{E}_{p(Z)} [\log(1 - f(D_{\theta_D}(G(M(Z)))))] \\ -\mathbb{E}_{p(x_r)} [\log(f(D_{\theta_D}(x_r)))] \\ + \frac{\eta}{2} \mathbb{E}_{p(x_r)} [\|\nabla D_{\theta_D}(x_r)\|^2] \quad (14)$$

where x_r denotes real MR images, η is the regularization parameter, and θ_D are the network weights for the discriminator.

Zero-Shot Reconstruction: Zero-shot or zero-data learning is a term first coined for classification tasks where a learning-based model is used to detect a novel class whose instances were absent from the training set. In this paper, we adopt the zero-shot learning approach to reduce dependency on training data for MRI reconstructions [60], [61]. To do this, we perform unsupervised pretraining of the style-generative model in SLATER to capture the distributional statistics of fully-sampled MRI data. This type of pretraining does not involve any prior information about the reconstruction task, so it can better generalize across tasks.

The generative model is then adapted to perform MRI reconstructions from undersampled data. For improved performance, we optimize the network prior during inference. Specifically, we optimize noise components (n), latent variables (W) and weights (θ_G) of the synthesizer model. An important detail is that the same latents W are input to all network layers during pretraining, however layer-specific optimization of latents (W^1, W^2, \dots, W^{13}) is performed during inference. For this purpose, the following selective loss function is used across acquired subset of k-space samples in the test data:

$$L_R(W, n, \theta_G) = \lambda_1 \|F_u CG(W^1, W^2, \dots, W^{13}, n, \theta_G) - k_x\|_1 + \lambda_2 \|F_u CG(W^1, W^2, \dots, W^{13}, n, \theta_G) - k_x\|_2 \quad (15)$$

where \hat{R} : reconstructed image, k_x : acquired k-space coefficients, F_u : partial Fourier operator, G : synthesizer, n : noise components and θ_G : synthesizer weights.

IV. METHODS

A. Pretraining and Zero-Shot Reconstruction with SLATER

Unsupervised Pretraining: SLATER was first pretrained to map random noise and latent codes onto high-quality MR images. In the IXI dataset, the model was trained to map onto single-coil magnitude images. In fastMRI dataset, the model was instead trained to map onto coil-combined complex images, with real and imaginary channel outputs. To do this, coil-combination was performed on multi-coil complex images using coil sensitivity maps derived via ESPIRiT with default parameters [76]. Subnetworks in SLATER were trained to minimize loss functions in Eqs. 10, 13 and 14, via Adam optimizer with parameters β_1 : 0.0, β_2 : 0.99 and ϵ : $1e^{-08}$ and regularization parameter used in Discriminator is $\eta = 10$. Model training was continued for a total of 10000 epochs, where intermediate checkpoints were saved for later selection. Separate SLATER models were trained to build MRI priors for each tissue contrast within each dataset.

Zero-Shot Reconstruction: Reconstruction was then performed via inference on individual test data conditioned by the MRI prior. Hyperparameter optimization was performed via cross-validation on a three-way split of subjects. The optimal checkpoint of the model from the pretraining stage and number of iterations for reconstruction were selected

to minimize the reconstruction loss. For IXI dataset, the checkpoint for the 470th pretraining epoch and regularization parameters $\lambda_1 = 1, \lambda_2 = 0$; for fastMRI, the checkpoint for the 1280th pretraining epoch and $\lambda_1 = 0.5, \lambda_2 = 0.5$ were selected. For all datasets, RMSprop optimizer was used for 1000 iterations. The same set of hyperparameters yielded near-optimal results in all cases. Following the final iteration, strict data consistency was enforced. For fastMRI, reconstructed images were projected onto individual coils, and the loss function in Eq. 15 was defined based on individual coils.

B. Competing Methods

To demonstrate SLATER, we compared it with several state-of-the-art techniques based on supervised and unsupervised models. Hyperparameter optimization was performed for each competing method via cross-validation as in SLATER. Detailed hyperparameter selections are provided in Supp. Text.

GAN_{sup}: A fully-supervised conditional generative adversarial network (GAN_{sup}) was trained using paired ground-truth and undersampled acquisitions. Generator and discriminator architectures were adopted from [28]. The generator was trained to minimize pixel-wise, perceptual, and adversarial losses between the reconstructed and reference images. A separate GAN_{sup} model was trained for each contrast within each dataset and acceleration rate.

SSDU: A self-supervised version of the conditional GAN model in GAN_{sup} was trained solely on undersampled data as described in [45]. Acquired k-space samples were split into two sets of nonoverlapping points, where 60% of samples were used to estimate model weights and 40% were used to define the network loss. All other training procedures were identical to GAN_{sup}. Separate SSDU models were trained for each contrast within each dataset and acceleration rate.

GAN_{prior}: Following [60], unsupervised pretraining on fully-sampled MR images was performed using an unconditional GAN model. Network architecture was adopted from [65] to enable a fair comparison against SLATER. Training and inference procedures were almost identical to those for SLATER with minor modifications explained in Supp. Text. Separate GAN_{prior} models were trained for each contrast within each dataset.

SAGAN: Zero-shot learned reconstructions were also implemented using a self-attention GAN model. The network architecture was adopted from [65]. Due to high computational cost of self-attention blocks, self-attention was only used at 32x32 resolution (4th network layer). Training and inference procedures were identical to those for SLATER. Separate models were trained for each contrast within each dataset.

GAN_{DIP}: DIP-type reconstructions were performed via the unconditional model in GAN_{prior} by omitting unsupervised pre-training.

SAGAN_{DIP}: DIP reconstructions were performed via a randomly initialized SAGAN model. Inference procedures were identical to SLATER.

SLATER_{DIP}: DIP reconstructions were performed based on a randomly initialized version of SLATER. Inference procedures were identical to SLATER.

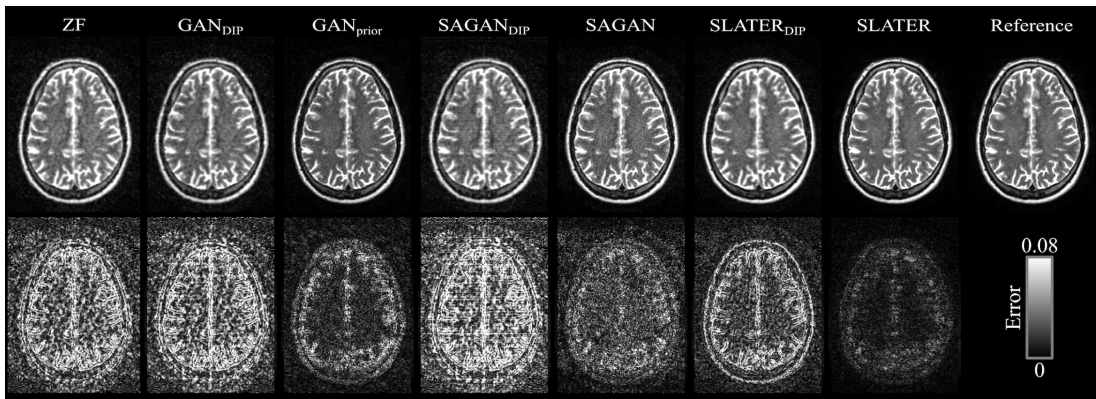


Fig. 3: Reconstructions of a representative T_2 -weighted acquisition at $R=4$ are shown for the Fourier method (ZF), DIP methods (GAN_{DIP} , $SAGAN_{DIP}$, $SLATER_{DIP}$) and zero-shot reconstructions (GAN_{prior} , SAGAN, SLATER) along with the reference image. Corresponding error maps are underneath the images for each method.

C. Datasets

Two public brain MRI datasets were used in the experiments reported here. Demonstrations were performed on single-coil data from IXI (<http://brain-development.org/ixi-dataset/>) and multi-coil data from fastMRI [77]. In IXI, T_1 -weighted and T_2 -weighted acquisitions were considered. Data from 40 subjects were analyzed, where 25 subjects were used for training, 5 for validation and 10 for testing. The scan protocol for T_1 -weighted acquisitions was: repetition time (TR)=9.813 ms, echo time (TE)=4.603 ms, flip angle=8°, matrix size=256x256x150, voxel size=0.94x0.94x1.2 mm³. For T_2 -weighted acquisitions: TR=8178 ms, TE=100 ms, flip angle=90°, matrix size=256x256x130, voxel size=0.94x0.94x1.2 mm³. In fastMRI, T_1 -weighted and T_2 -weighted acquisitions were considered. Data from 150 subjects were analyzed, where 100 subjects were used for training, 10 for validation and 40 for testing. There is no common protocol in fastMRI as data were acquired at multiple sites. Only volumes with at least 10 cross-sections and acquired with at least 5 coils were selected. To reduce computational complexity, GCC [78] was used to decrease the number of coils to 5. For both datasets, subject selection and splitting was done sequentially. Data were retrospectively undersampled using variable-density random patterns [3]. Undersampling masks were generated based on a 2D normal distribution with covariance adaptively adjusted to obtain the desired acceleration rates of $R=[4x, 8x]$.

D. Quantitative Assessments

To assess reconstruction quality, quantitative comparisons were performed against reference images Fourier-reconstructed from fully-sampled acquisitions. Both reconstructed and reference images were normalized to a maximum of 1 prior to measurement. Peak signal-to-noise ratio (PSNR) and structural similarity index (SSIM) were calculated between the reconstructed and reference images. In Tables, summary statistics for quantitative metrics were provided as mean \pm standard deviation across test subjects. Statistical significance of differences between methods were assessed via a nonparametric Wilcoxon signed-rank test.

V. RESULTS

A. Model Invertability

During inference on test data, SLATER inverts its generative model to identify noise, latents and network weights that are most consistent with the undersampled MRI acquisition. To evaluate model invertability, we compared SLATER against CNN-based and self-attention GAN models. Each model was used in both DIP and zero-shot reconstructions. Representative results on T_1 - and T_2 -weighted images from the IXI dataset at $R=4$ are displayed in Fig. 3 and Supp. Fig. 1 respectively. DIP reconstructions tend to suffer from visible loss of spatial resolution, and GAN_{prior} and SAGAN have elevated noise and artifacts. In contrast, SLATER yields low residual errors and high visual acuity. Quantitative performance metrics are listed in Table I. SLATER achieves superior performance against GAN_{prior} and SAGAN in both DIP and zero-shot reconstructions ($p < 0.05$). Compared to the second-best method, SLATER yields 4.36dB higher PSNR and 7.65% higher SSIM in DIP, and 4.46dB higher PSNR and 7.16% higher SSIM in zero-shot reconstruction. Furthermore, SLATER yields 5.14dB higher PSNR and 6.92% higher SSIM over $SLATER_{DIP}$. These results indicate that the cross-attention transformer blocks in SLATER enhance model invertability compared to CNN-based GAN architectures with or without self-attention blocks and that the unsupervised pretraining stage in SLATER improves convergence.

B. Within-Domain Reconstructions

Next, we assessed within-domain reconstruction performance. This meant that the training and testing domains matched (e.g., T_1 reconstruction based on a T_1 -prior for SLATER). SLATER was compared against GAN_{sup} , SSDU, GAN_{prior} and SAGAN at $R=4$ and 8. Representative reconstructions are shown for IXI in Fig. 4 and Supp. Fig. 2, and for fastMRI in Fig. 5 and Supp. Fig. 3. SLATER yields lower residual errors and higher acuity in depicting detailed tissue structure than competing methods. Quantitative assessments are listed in Tables II and III. SLATER achieves significantly

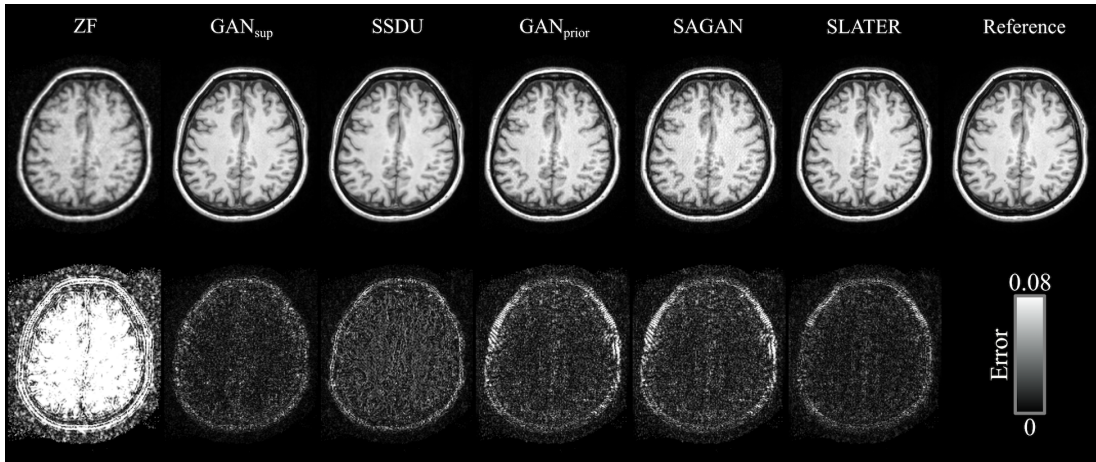


Fig. 4: Within-domain reconstructions of a T_1 -weighted acquisition in the IXI dataset at $R=4$ are shown for the Fourier method (ZF), a supervised baseline (GAN_{sup}), unsupervised baselines (SSDU, GAN_{prior} , SAGAN) and the proposed method (SLATER) along with the reference image. Corresponding error maps are underneath the images for each method.

TABLE I: Reconstruction performance of DIP and zero-shot reconstructions for T_1 - and T_2 -weighted images in the IXI dataset at $R=4$ and 8. Results are displayed for GAN_{prior} , SAGAN, SLATER and their DIP variants, and ZF along with the reference image. Corresponding error maps are underneath the images for each method.

	GAN_{DIP}		$SAGAN_{DIP}$		$SLATER_{DIP}$		GAN_{prior}		SAGAN		SLATER	
	PSNR	SSIM(%)	PSNR	SSIM(%)	PSNR	SSIM(%)	PSNR	SSIM(%)	PSNR	SSIM(%)	PSNR	SSIM(%)
T_1 , $R=4$	26.67±1.22	87.37±0.99	26.60±1.10	86.48±0.99	32.55±1.77	94.58±0.82	34.36±0.83	94.44±0.66	31.25±1.16	91.44±0.98	38.75±0.83	97.86±0.46
T_1 , $R=8$	23.45±0.92	83.02±1.13	23.42±0.90	82.50±1.17	30.28±1.68	91.64±1.42	29.28±1.17	89.67±1.43	27.68±0.98	87.42±1.17	33.24±0.86	95.20±0.85
T_2 , $R=4$	30.23±0.45	80.77±1.22	29.90±0.40	79.41±1.36	32.71±0.73	87.66±1.67	33.43±0.87	87.54±1.02	34.55±0.94	88.97±1.93	40.00±0.79	97.72±0.49
T_2 , $R=8$	27.64±0.38	76.16±1.30	27.28±0.37	74.06±1.57	29.90±0.70	84.03±1.89	31.15±0.74	85.29±1.02	30.33±0.67	83.07±1.84	34.07±0.75	94.80±0.66

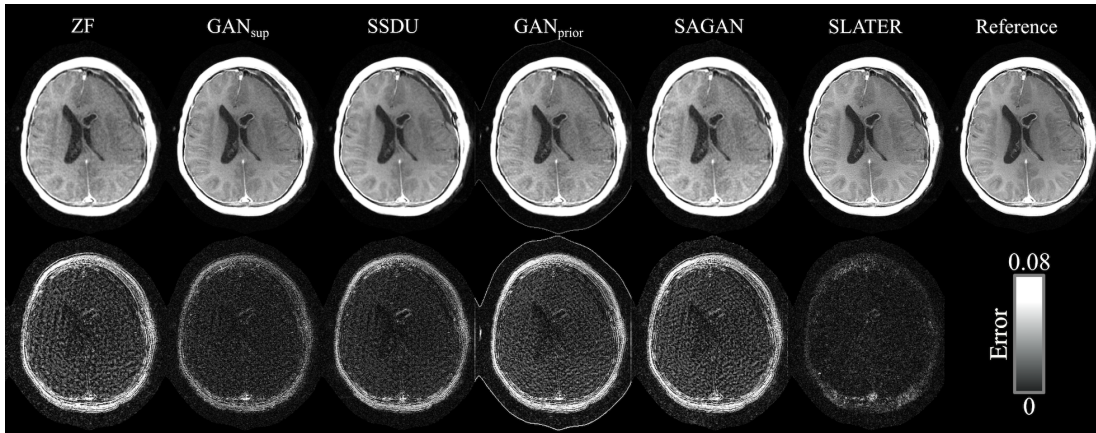


Fig. 5: Within-domain reconstructions of a T_1 -weighted acquisition in the fastMRI dataset at $R=4$. Results are shown for ZF, GAN_{sup} , SSDU, GAN_{prior} , SAGAN and SLATER along with the reference image. Corresponding error maps are underneath the images for each method.

TABLE II: Within-domain reconstruction performance for T_1 - and T_2 -weighted images in the IXI dataset at $R=4$ and 8.

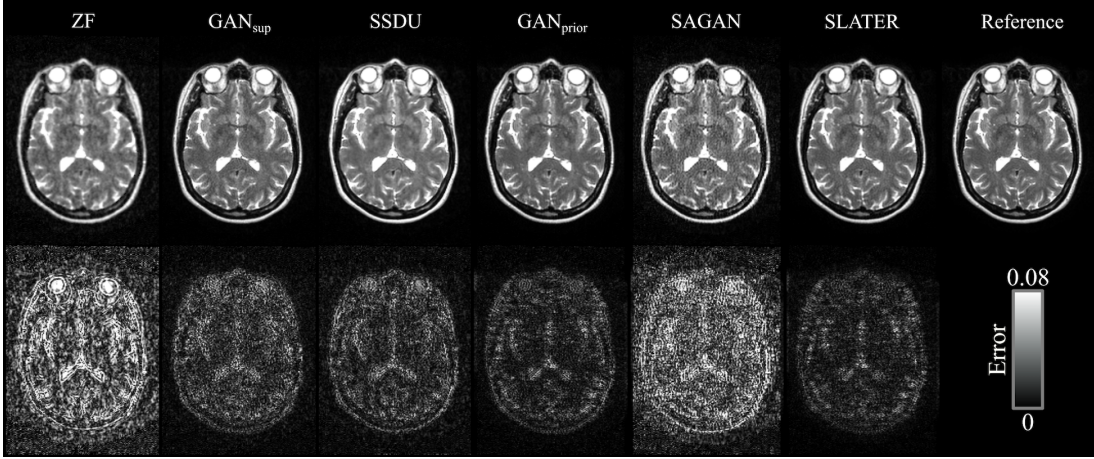
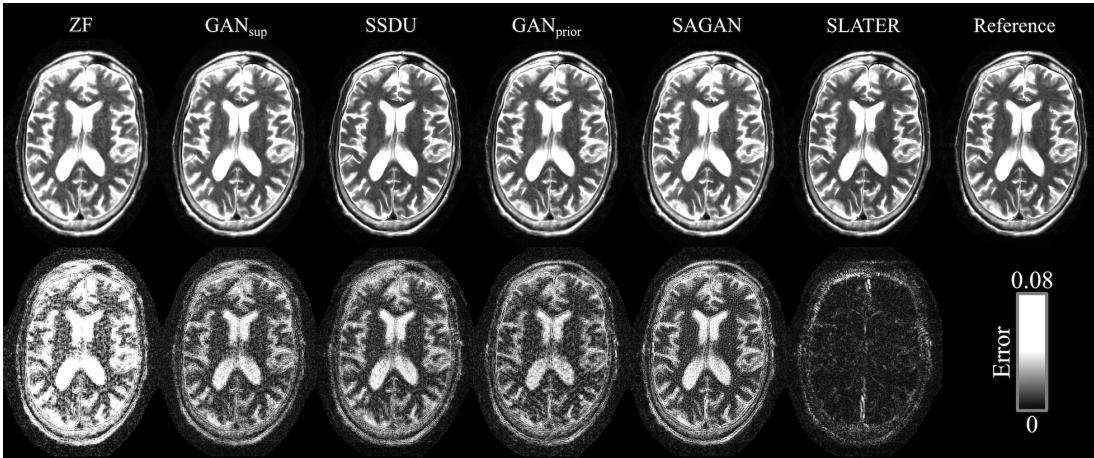
	GAN_{sup}		SSDU		GAN_{prior}		SAGAN		SLATER	
	PSNR	SSIM(%)	PSNR	SSIM(%)	PSNR	SSIM(%)	PSNR	SSIM(%)	PSNR	SSIM(%)
T_1 , $R=4$	37.47±0.53	97.80±0.18	37.94±0.61	97.77±0.18	34.36±0.83	94.44±0.66	31.25±1.16	91.44±0.98	38.75±0.83	97.86±0.46
T_1 , $R=8$	33.25±0.59	95.73±0.31	33.12±0.72	93.92±0.71	29.28±1.17	89.67±1.43	27.68±0.98	87.42±1.17	33.24±0.86	95.20±0.85
T_2 , $R=4$	38.65±0.75	96.76±0.34	38.90±0.71	96.34±0.44	33.43±0.87	87.54±1.02	34.55±0.94	88.96±1.93	40.00±0.79	97.72±0.49
T_2 , $R=8$	34.22±0.80	94.31±0.60	33.74±0.86	91.64±1.12	31.15±0.74	85.29±1.02	30.33±0.67	83.07±1.84	34.07±0.75	94.80±0.66

enhanced reconstruction quality against all competing unsupervised methods ($p < 0.05$) offering 1.05dB higher PSNR and 1.08% higher SSIM compared to the second-best method. Furthermore, it offers 4.42dB higher PSNR and 5.54% higher SSIM compared to the GAN_{prior} . It also yields higher perfor-

mance than GAN_{sup} in all tasks ($p < 0.05$), except at $R=8$ in IXI where the two methods perform similarly and $R=8$ in fastMRI where GAN_{sup} yields higher SSIM. These results indicate that SLATER offers enhanced reconstruction quality for within-domain tasks compared to competing unsupervised

TABLE III: Within-domain reconstruction performance for T_1 - and T_2 -weighted images in the fastMRI dataset at R=4 and 8.

	GAN _{sup}		SSDU		GAN _{prior}		SAGAN		SLATER	
	PSNR	SSIM(%)	PSNR	SSIM(%)	PSNR	SSIM(%)	PSNR	SSIM(%)	PSNR	SSIM(%)
T_1 , R=4	37.24±2.55	94.43±5.72	37.24±3.27	94.23±7.54	32.76±1.97	92.50±5.23	34.69±2.60	94.44±5.34	37.64±3.18	93.92±9.47
T_1 , R=8	34.59±2.38	92.04±6.95	33.86±2.60	90.56±8.47	29.77±1.92	88.34±6.74	32.30±2.37	90.71±6.90	34.15±2.40	90.65±7.90
T_2 , R=4	35.37±1.17	95.49±0.52	32.99±2.85	94.63±1.27	33.45±1.06	91.46±1.80	32.49±1.43	93.27±1.06	36.29±1.20	95.54±0.69
T_2 , R=8	32.67±1.29	93.04±0.82	31.34±1.29	90.99±1.50	27.96±1.37	85.10±2.48	30.27±1.39	90.01±1.49	33.36±1.13	92.99±0.98

**Fig. 6:** Across-domain reconstructions of a T_2 -weighted acquisition in the IXI dataset at R=4. Results are shown for ZF, GAN_{sup}, SSDU, GAN_{prior}, SAGAN and SLATER along with the reference image. Corresponding error maps are underneath the images for each method.**Fig. 7:** Across-domain reconstructions of a T_2 -weighted acquisition in the fastMRI dataset at R=4. Results are shown for ZF, GAN_{sup}, SSDU, GAN_{prior}, SAGAN and SLATER along with the reference image. Corresponding error maps are underneath the images for each method.

methods, while offering on par performance to a supervised baseline.

C. Across-Domain Reconstructions

We then evaluated across-domain reconstruction performance of SLATER, when the test domain was different than the domain of the MRI prior (e.g., T_2 reconstructions based on a T_1 -prior). SLATER was compared against GAN_{sup}, SSDU, GAN_{prior} and SAGAN at R=4. Representative reconstructions are shown for IXI in Fig. 6 and Supp. Fig. 4, and for fastMRI in Fig 7. and Supp. Fig. 5. Again, SLATER yields lower residual errors and higher acuity in depicting detailed tissue

structure than competing methods. Quantitative assessments are listed in Tables IV and V. SLATER achieves superior reconstruction quality against all competing supervised and unsupervised methods ($p < 0.05$), offering 2.50dB higher PSNR and 1.54% higher SSIM compared to the second-best method. Furthermore, it offers 3.62dB higher PSNR and 3.89% higher SSIM compared to the GAN_{prior}. These results demonstrate that SLATER has improved generalization capabilities compared to static supervised and unsupervised models with fixed weights during inference.

TABLE IV: Across-domain reconstruction performance for T_1 - and T_2 -weighted images in the IXI dataset at $R=4$. In $A \rightarrow B$, A is the training domain and B is the test domain.

	GAN_{sup}		SSDU		$\text{GAN}_{\text{prior}}$		SAGAN		SLATER	
	PSNR	SSIM(%)	PSNR	SSIM(%)	PSNR	SSIM(%)	PSNR	SSIM(%)	PSNR	SSIM(%)
$T_1 \rightarrow T_2$	36.75 \pm 0.72	95.30 \pm 0.57	34.81 \pm 0.95	90.34 \pm 1.35	36.36 \pm 0.70	93.22 \pm 0.56	31.99 \pm 0.59	85.46 \pm 1.19	39.86 \pm 0.80	97.68 \pm 0.50
$T_2 \rightarrow T_1$	35.32 \pm 0.58	96.35 \pm 0.26	35.67 \pm 0.41	96.25 \pm 0.30	32.51 \pm 0.96	91.64 \pm 1.12	33.17 \pm 0.74	91.99 \pm 0.68	38.74 \pm 0.91	97.87 \pm 0.47

TABLE V: Across-domain reconstruction performance for T_1 - and T_2 -weighted images in the fastMRI dataset at $R=4$.

	GAN_{sup}		SSDU		$\text{GAN}_{\text{prior}}$		SAGAN		SLATER	
	PSNR	SSIM(%)	PSNR	SSIM(%)	PSNR	SSIM(%)	PSNR	SSIM(%)	PSNR	SSIM(%)
$T_1 \rightarrow T_2$	33.79 \pm 1.15	94.13 \pm 0.70	34.79 \pm 1.13	95.13 \pm 0.65	33.46 \pm 1.45	94.31 \pm 0.83	32.78 \pm 1.57	94.01 \pm 1.12	36.16 \pm 1.08	94.64 \pm 0.99
$T_2 \rightarrow T_1$	36.85 \pm 2.39	93.55 \pm 5.75	34.33 \pm 3.33	92.90 \pm 9.15	35.90 \pm 2.09	90.78 \pm 5.41	33.96 \pm 2.25	93.69 \pm 5.28	37.96 \pm 2.56	95.30 \pm 6.17

TABLE VI: Reconstruction performance in ablation experiments for SLATER. Metrics are reported for T_1 - and T_2 - weighted images in the IXI dataset at $R=4$.

	None		Latent		Latent + Noise		Latent + Noise + Weight	
	PSNR	SSIM(%)	PSNR	SSIM(%)	PSNR	SSIM(%)	PSNR	SSIM(%)
T_1	26.73 \pm 1.28	87.10 \pm 1.23	32.40 \pm 1.13	94.08 \pm 0.65	33.97 \pm 1.18	96.60 \pm 0.36	38.75 \pm 0.83	97.86 \pm 0.46
T_2	30.44 \pm 0.67	80.51 \pm 1.39	32.86 \pm 0.76	87.99 \pm 0.85	36.18 \pm 0.79	94.29 \pm 0.58	40.00 \pm 0.79	97.72 \pm 0.49

D. Ablation Experiments

Lastly, we examined the contributions of individual components in SLATER that are optimized during inference. To do this, variant models were built by progressively introducing optimization for latent variables, noise and network weights. Experiments were conducted on T_1 - and T_2 -weighted acquisitions in the IXI dataset at $R=4$. Table VI lists quantitative performance metrics where optimization was performed for none of the components, latents, latents and noise, and all three components. On average, the incurred performance gain in (PSNR, SSIM) is (4.05dB, 7.23%) with latent optimization, (6.50dB, 11.64%) with latent and noise optimization, and (10.80dB, 13.99%) with latent, noise and weight optimization. These results indicate the importance of each component in SLATER.

VI. DISCUSSION

In this study, we propose a novel unsupervised reconstruction technique (SLATER) for multi-coil undersampled MRI acquisitions, based on deep generative modeling and zero-shot learning. Our framework rests on a style-generative deep adversarial network that maps noise and latent variables onto MR images. This choice is motivated by prior computer vision studies suggesting that intermediate latent spaces connected to individual network layers in the synthesizer significantly improve feature control [62], [65]. The adversarial network further employs cross-attention transformer blocks to improve capture of contextual relations between latent variables and image features. SLATER first performs unsupervised pretraining of the adversarial network to learn high-quality MR priors. It then performs zero-shot reconstruction of undersampled acquisitions by adapting these priors to test data in a reverse inference procedure.

To our knowledge, this is the first study to introduce an adversarial transformer network for MRI reconstruction. Traditional GAN models are constructed via cascades of convolutional layers. The limited size of convolutional kernels in turn limit the ability to capture long-range spatial dependencies. To

enhance capture of local and global context, here we employed an adversarial network with cross-attention transformer blocks. These blocks enable dynamic routing of information latent variables and features to improve controllability of generated MR images. Note that vanilla transformers with self-attention among all features would lead to excessive computational burden [79], [80]. To address this limitation, we leverage an efficient implementation that prunes attention to a compact set of latents to prevent quadratic complexity [66]. Recent studies have proposed self-attention modules tied to the output of convolutional layers in CNN-based models for medical image processing [67], [81]–[85]. The attention modules were inserted to the output of convolutional layers to modify feature maps containing only local information. Note that self-attention modules suffer from quadratic complexity, and so they are used only in network layers with relatively modest resolution. Instead, here we used cross-attention with compact support to permit use at higher resolutions.

Comprehensive demonstrations on single- and multi-coil datasets clearly indicate the superiority of the proposed method over several state-of-the-art methods. The competing methods include a fully-supervised conditional GAN model (GAN_{sup}), a recent self-supervised training method (SSDU), DIP reconstructions based on CNN-based and self-attention GANs (GAN_{DIP} , $\text{SAGAN}_{\text{DIP}}$), and zero-shot reconstructions ($\text{GAN}_{\text{prior}}$, SAGAN). SLATER offers on par performance with GAN_{sup} in terms of quantitative metrics and visual depictions of tissue structure for within-domain tasks, while it outperforms GAN_{sup} for across-domain tasks. SLATER also outperforms unsupervised DIP methods by a substantial margin, which can be attributed to the unsupervised pretraining stage. Lastly, SLATER yields superior performance to $\text{GAN}_{\text{prior}}$ that indicates the importance of transformer blocks in learning a high-fidelity prior.

Several recent studies have considered unpaired or unsupervised learning methods for MRI reconstruction. A successful approach has been to devise learning strategies that only require unpaired samples of undersampled and fully-sampled

MRI acquisitions [38]–[40]. Compared to unpaired techniques, SLATER does not use fully-sampled MRI data to train its network model under the reconstruction task, but instead performs unsupervised training in a self-encoding task. Importantly, SLATER successfully generalizes when the MRI prior and undersampled test data come from different domains, so it has relaxed training requirements. Another highly promising approach is to train reconstruction models via self-supervision methods on undersampled data, and to fix the model weights during inference on test samples [42], [44]–[46], [48]–[52]. This unsupervised approach eliminates the need for collection of reference datasets. A main difference of SLATER is that it performs test-sample specific adaptation of its reconstruction model for elevated performance, at the expense of longer inference times.

Among recent efforts, the closest to the presented approach are methods based on the DIP framework [68]. Compared to mainstream DIP that uses randomly initialized networks, here we show that reconstructions can be significantly enhanced by using a prelearned network that captures high-quality MR priors. A similar strategy has been proposed in [61] that uses a variational auto-encoder to learn patch priors and [60] that uses a GAN to learn image priors. Our work differs from these previous efforts in the following aspects: (i) Compared to [61] that uses a computationally simpler patch-based implementation, we leverage an image-based implementation that might improve performance in leveraging broader, non-local context. (ii) [61] uses a fixed patch prior during inference, whereas we perform test-sample specific adaptation of the MR prior (iii) Compared to [60] that uses a CNN-based GAN architecture, here we use an architecture with cross-attention transformers to better capture long-range spatial dependencies. (iv) SLATER additionally includes noise and latent variables injected at each level of the synthesizer network to allow better control of the reconstructed image, as demonstrated by the ablation experiments.

There are several lines of methodological development that can be pursued for the proposed framework. First, as opposed to mapping from randomly initialized noise and latent variables, the model can be map from initial estimates of noise and latent variables. These estimates can be derived via traditional parallel imaging/compressed sensing reconstructions [72], and a mapping network can be trained to find the image to latent transformation for the output of traditional methods. This can increase the computational efficiency of SLATER by shortening the inference procedure, depending on the time it takes to produce the initial estimates. Second, it might possible to combine the reconstruction loss in SLATER with SURE-type estimates of reconstruction error or regularization terms on network weights [52]. Here we did not explicitly regularize the weights, latents or noise to allow higher degree of consistency to acquired data. When desired, network regularization and on-line error estimates can be introduced to reduce potential for overfitting.

VII. CONCLUSION

Here we introduced a zero-shot learned adversarial transformer network for unsupervised MRI reconstruction. Quan-

titative and qualitative benefits of the proposed approach over several state-of-the-art unsupervised methods were demonstrated on brain MRI datasets. The proposed approach can also be adopted for structural and dynamic MRI in other anatomies, or leveraged for unsupervised reconstruction in imaging modalities such as CT. Alleviation of data requirements in model training and subject-specific adaptation of the reconstruction model render SLATER a promising candidate for high-performance MRI reconstructions in practice.

REFERENCES

- [1] K. P. Pruessmann, M. Weiger, M. B. Scheidegger, and P. Boesiger, "SENSE: sensitivity encoding for fast MRI." *Magnetic Resonance in Medicine*, vol. 42, no. 5, pp. 952–62, 1999.
- [2] M. A. Griswold, P. M. Jakob, R. M. Heidemann, M. Nittka, V. Jellus, J. Wang, B. Kiefer, and A. Haase, "Generalized autocalibrating partially parallel acquisitions (GRAPPA)." *Magnetic Resonance in Medicine*, vol. 47, no. 6, pp. 1202–1210, 2002.
- [3] M. Lustig, D. Donoho, and J. M. Pauly, "Sparse MRI: The application of compressed sensing for rapid MR imaging." *Magnetic Resonance in Medicine*, vol. 58, no. 6, pp. 1182–1195, 2007.
- [4] M. Lustig and J. M. Pauly, "SPIRiT: Iterative self-consistent parallel imaging reconstruction from arbitrary k-space." *Magnetic Resonance in Medicine*, vol. 64, no. 2, pp. 457–71, 2010.
- [5] D. Liang, J. Cheng, Z. Ke, and L. Ying, "Deep Magnetic Resonance Image reconstruction: Inverse problems meet neural networks." *IEEE Signal Processing Magazine*, vol. 37, no. 1, pp. 141–151, 2020.
- [6] C. M. Sandino, J. Y. Cheng, F. Chen, M. Mardani, J. M. Pauly, and S. S. Vasanawala, "Compressed sensing: From research to clinical practice with deep neural networks: Shortening scan times for Magnetic Resonance Imaging." *IEEE Signal Processing Magazine*, vol. 37, no. 1, pp. 117–127, 2020.
- [7] C. M. Hyun, H. P. Kim, S. M. Lee, S. Lee, and J. K. Seo, "Deep learning for undersampled MRI reconstruction." *Physics in Medicine and Biology*, vol. 63, no. 13, p. 135007, 2018.
- [8] S. Wang, Z. Su, L. Ying, X. Peng, S. Zhu, F. Liang, D. Feng, and D. Liang, "Accelerating magnetic resonance imaging via deep learning." in *IEEE 13th International Symposium on Biomedical Imaging (ISBI)*, 2016, pp. 514–517.
- [9] J. Yoon, E. Gong, I. Chatnuntawech, B. Bilgic, J. Lee, W. Jung, J. Ko, H. Jung, K. Setsompop, G. Zaharchuk, E. Y. Kim, J. Pauly, and J. Lee, "Quantitative susceptibility mapping using deep neural network: QSMnet." *NeuroImage*, vol. 179, pp. 199–206, 2018.
- [10] D. Lee, J. Yoo, S. Tak, and J. C. Ye, "Deep residual learning for accelerated MRI using magnitude and phase networks." *IEEE Transactions on Biomedical Engineering*, vol. 65, no. 9, pp. 1985–1995, 2018.
- [11] A. Hauptmann, S. Arridge, F. Lucka, V. Muthurangu, and J. A. Steeden, "Real-time cardiovascular MR with spatio-temporal artifact suppression using deep learning—proof of concept in congenital heart disease." *Magnetic Resonance in Medicine*, vol. 81, no. 2, pp. 1143–1156, 2019.
- [12] K. Kwon, D. Kim, and H. Park, "A parallel MR imaging method using multilayer perceptron." *Medical Physics*, vol. 44, no. 12, pp. 6209–6224, 2017.
- [13] B. Zhu, J. Z. Liu, B. R. Rosen, and M. S. Rosen, "Image reconstruction by domain transform manifold learning." *Nature*, vol. 555, no. 7697, pp. 487–492, 2018.
- [14] J. Schlemper, J. Caballero, J. V. Hajnal, A. Price, and D. Rueckert, "A Deep Cascade of Convolutional Neural Networks for MR Image Reconstruction." in *International Conference on Information Processing in Medical Imaging*, 2017, pp. 647–658.
- [15] Y. Yang, J. Sun, H. Li, and Z. Xu, "Deep ADMM-Net for compressive sensing MRI." in *Advances in Neural Information Processing Systems*, vol. 29, 2016.
- [16] H. K. Aggarwal, M. P. Mani, and M. Jacob, "MoDL: Model-Based deep learning architecture for inverse problems." *IEEE Transactions on Medical Imaging*, vol. 38, no. 2, pp. 394–405, 2019.
- [17] Y. Yang, J. Sun, H. Li, and Z. Xu, "ADMM-CSNet: A deep learning approach for image compressive sensing." *IEEE Transactions on Pattern Analysis and Machine Intelligence*, vol. 42, no. 3, pp. 521–538, 2020.
- [18] T. Eo, Y. Jun, T. Kim, J. Jang, H.-J. Lee, and D. Hwang, "KIKI-net: cross-domain convolutional neural networks for reconstructing under-sampled magnetic resonance images." *Magnetic Resonance in Medicine*, vol. 80, no. 5, pp. 2188–2201, 2018.

- [19] J. Cheng, H. Wang, L. Ying, and D. Liang, "Model learning: Primal dual networks for fast MR imaging," in *Proceedings of MICCAI*, 2019, pp. 21–29.
- [20] J. Adler and O. Öktem, "Learned primal-dual reconstruction," *IEEE Transactions on Medical Imaging*, vol. 37, no. 6, pp. 1322–1332, 2018.
- [21] S. Wang, Z. Ke, H. Cheng, S. Jia, L. Ying, H. Zheng, and D. Liang, "DIMENSION: Dynamic MR imaging with both k-space and spatial prior knowledge obtained via multi-supervised network training," *NMR in Biomedicine*, p. e4131, 2019.
- [22] S. A. H. Hosseini, B. Yaman, S. Moeller, M. Hong, and M. Akçakaya, "Dense recurrent neural networks for accelerated MRI: History-cognizant unrolling of optimization algorithms," *IEEE Journal of Selected Topics in Signal Processing*, vol. 14, no. 6, pp. 1280–1291, 2020.
- [23] C. Qin, J. Schlemper, J. Caballero, A. N. Price, J. V. Hajnal, and D. Rueckert, "Convolutional recurrent neural networks for dynamic MR image reconstruction," *IEEE Transactions on Medical Imaging*, vol. 38, no. 1, pp. 280–290, 2019.
- [24] M. Mardani, E. Gong, J. Y. Cheng, S. Vasanawala, G. Zaharchuk, L. Xing, and J. M. Pauly, "Deep generative adversarial neural networks for compressive sensing MRI," *IEEE Transactions on Medical Imaging*, vol. 38, no. 1, pp. 167–179, 2019.
- [25] Y. Chen, D. Firmin, and G. Yang, "Wavelet improved GAN for MRI reconstruction," in *Proceedings of SPIE, Medical Imaging 2021: Physics of Medical Imaging*, vol. 11595, 2021, p. 1159513.
- [26] S. Yu, H. Dong, G. Yang, G. Slabaugh, P. L. Dragotti, X. Ye, F. Liu, S. Arridge, J. Keegan, D. Firmin, and Y. Guo, "DAGAN: Deep de-aliasing generative adversarial networks for fast compressed sensing MRI reconstruction," *IEEE Transactions on Medical Imaging*, vol. 37, no. 6, pp. 1310–1321, 2018.
- [27] M. Mardani, H. Monajemi, V. Pappayan, S. Vasanawala, D. Donoho, and J. Pauly, "Recurrent generative adversarial networks for proximal learning and automated compressive image recovery," *arXiv preprint arXiv:1711.10046*, 2017.
- [28] S. U. Dar, M. Yurt, M. Shahdloo, M. E. Ildiz, B. Tınaz, and T. Çukur, "Prior-guided image reconstruction for accelerated multi-contrast MRI via generative adversarial networks," *IEEE Journal of Selected Topics in Signal Processing*, vol. 14, no. 6, pp. 1072–1087, 2020.
- [29] J. C. Ye, Y. Han, and E. Cha, "Deep convolutional framelets: A general deep learning framework for inverse problems," *SIAM Journal on Imaging Sciences*, vol. 11, no. 2, pp. 991–1048, 2018.
- [30] K. Hammernik, T. Klatzer, E. Kobler, M. P. Recht, D. K. Sodickson, T. Pock, and F. Knoll, "Learning a variational network for reconstruction of accelerated MRI data," *Magnetic Resonance in Medicine*, vol. 79, no. 6, pp. 3055–3071, 2017.
- [31] F. Knoll, K. Hammernik, E. Kobler, T. Pock, M. P. Recht, and D. K. Sodickson, "Assessment of the generalization of learned image reconstruction and the potential for transfer learning," *Magnetic Resonance in Medicine*, vol. 81, no. 1, pp. 116–128, 2019.
- [32] D. Polak, S. Cauley, B. Bilgic, E. Gong, P. Bachert, E. Adalsteinsson, and K. Setsompop, "Joint multi-contrast variational network reconstruction (jVN) with application to rapid 2D and 3D imaging," *Magnetic Resonance in Medicine*, vol. 84, no. 3, pp. 1456–1469, 2020.
- [33] A. Sriram, J. Zbontar, T. Murrell, A. Defazio, C. L. Zitnick, N. Yakubova, F. Knoll, and P. Johnson, "End-to-end variational networks for accelerated MRI reconstruction," in *Proceedings of MICCAI*, A. L. Martel, P. Abolmaesumi, D. Stoyanov, D. Mateus, M. A. Zuluaga, S. K. Zhou, D. Racoceanu, and L. Joskowicz, Eds., 2020, pp. 64–73.
- [34] Q. Chang, H. Qu, Y. Zhang, M. Sabuncu, C. Chen, T. Zhang, and D. N. Metaxas, "Synthetic learning: Learn from distributed asynchronous discriminator GAN without sharing medical image data," in *2020 IEEE/CVF Conference on Computer Vision and Pattern Recognition (CVPR)*, 2020, pp. 13 853–13 863.
- [35] Y. Han, J. Yoo, H. H. Kim, H. J. Shin, K. Sung, and J. C. Ye, "Deep learning with domain adaptation for accelerated projection-reconstruction MR," *Magnetic Resonance in Medicine*, vol. 80, no. 3, pp. 1189–1205, 2018.
- [36] S. U. H. Dar, M. Özbek, A. B. Çatlı, and T. Çukur, "A transfer-learning approach for accelerated MRI using deep neural networks," *Magnetic Resonance in Medicine*, vol. 84, no. 2, pp. 663–685, 2020.
- [37] S. U. Dar, M. Yurt, and T. Çukur, "A Few-Shot Learning Approach for Accelerated MRI via Fusion of Data-Driven and Subject-Driven Priors," in *Proceedings of the 29th Annual Meeting of the ISMRM*, 2021.
- [38] T. M. Quan, T. Nguyen-Duc, and W.-K. Jeong, "Compressed sensing MRI reconstruction with cyclic loss in generative adversarial networks," *IEEE Transactions on Medical Imaging*, vol. 37, no. 6, pp. 1488–1497, 2018.
- [39] G. Oh, B. Sim, H. Chung, L. Sunwoo, and J. C. Ye, "Unpaired deep learning for accelerated MRI using optimal transport driven cycleGAN," *IEEE Transactions on Computational Imaging*, vol. 6, pp. 1285–1296, 2020.
- [40] K. Lei, M. Mardani, J. M. Pauly, and S. S. Vasanawala, "Wasserstein gans for mr imaging: From paired to unpaired training," *IEEE Transactions on Medical Imaging*, vol. 40, no. 1, pp. 105–115, 2021.
- [41] H. Chung, E. Cha, L. Sunwoo, and J. C. Ye, "Two-stage deep learning for accelerated 3D time-of-flight MRA without matched training data," *Medical Image Analysis*, vol. 71, p. 102047, 2021.
- [42] J. I. Tamir, S. X. Yu, and M. Lustig, "Unsupervised deep basis pursuit: Learning reconstruction without ground-truth data," in *Proceedings of the 27th Annual Meeting of the ISMRM*, 2019, p. 0660.
- [43] A. Q. Wang, A. V. Dalca, and M. R. Sabuncu, "Neural network-based reconstruction in compressed sensing MRI without fully-sampled training data," in *Machine Learning for Medical Image Reconstruction*, 2020, pp. 27–37.
- [44] E. K. Cole, J. M. Pauly, S. S. Vasanawala, and F. Ong, "Unsupervised MRI reconstruction with generative adversarial networks," *arXiv preprint arXiv:2008.13065*, 2020.
- [45] B. Yaman, S. A. H. Hosseini, S. Moeller, J. Ellermann, K. Uğurbil, and M. Akçakaya, "Self-supervised learning of physics-guided reconstruction neural networks without fully sampled reference data," *Magnetic resonance in medicine*, vol. 84, no. 6, pp. 3172–3191, 2020.
- [46] P. Huang, C. H. Li, S. K. Gaire, R. Liu, X. Zhang, X. Li, and L. Ying, "Deep MRI reconstruction without ground truth for training," in *Proceedings of the 27th Annual Meeting of the ISMRM*, 2019, p. 4668.
- [47] B. Yaman, S. A. H. Hosseini, S. Moeller, J. Ellermann, K. Uğurbil, and M. Akçakaya, "Multi-mask self-supervised learning for physics-guided neural networks in highly accelerated MRI," *arXiv preprint arXiv:2008.06029*, 2020.
- [48] J. Liu, Y. Sun, C. Eldeniz, W. Gan, H. An, and U. S. Kamilov, "RARE: Image reconstruction using deep priors learned without groundtruth," *IEEE Journal of Selected Topics in Signal Processing*, vol. 14, no. 6, pp. 1088–1099, 2020.
- [49] J. Liu, C. Eldeniz, W. Sun, Yu Gan, S. Chen, H. An, and U. S. Kamilov, "RED-N2N: Image reconstruction for MRI using deep CNN priors trained without ground truth," in *Proceedings of the 28th Annual Meeting of the ISMRM*, 2020, p. 0993.
- [50] C. Eldeniz, W. Gan, S. Chen, J. Liu, U. S. Kamilov, and H. An, "Phase2Phase: Reconstruction of free-breathing MRI into multiple respiratory phases using deep learning without a ground truth," in *Proceedings of the 28th Annual Meeting of the ISMRM*, 2020, p. 0807.
- [51] P. Huang, C. Zhang, H. Li, S. K. Gaire, R. Liu, X. Zhang, X. Li, L. Dong, and L. Ying, "Unsupervised deep learning reconstruction using the MR imaging model," in *Proceedings of the 28th Annual Meeting of the ISMRM*, 2020, p. 3617.
- [52] H. K. Aggarwal and M. Jacob, "ENSURE: Ensemble Stein's unbiased risk estimator for unsupervised learning," *arXiv preprint arXiv:2010.10631*, 2020.
- [53] S. A. Hossein Hosseini, B. Yaman, S. Moeller, and M. Akçakaya, "High-fidelity accelerated MRI reconstruction by scan-specific fine-tuning of physics-based neural networks," in *Proceedings of the IEEE Engineering in Medicine Biology Society (EMBC)*, 2020, pp. 1481–1484.
- [54] H. K. Aggarwal and M. Jacob, "Model adaptation for image reconstruction using generalized Stein's unbiased risk estimator," *arXiv preprint arXiv:2102.00047*, 2021.
- [55] S. Biswas, H. K. Aggarwal, and M. Jacob, "Dynamic MRI using model-based deep learning and STORM priors: MoDL-SToRM," *Magnetic resonance in medicine*, vol. 82, no. 1, pp. 485–494, 2019.
- [56] K. H. Jin, H. Gupta, J. Yerly, M. Stuber, and M. Unser, "Time-dependent deep image prior for dynamic MRI," *arXiv preprint arXiv:1910.01684*, 2019.
- [57] S. Arora, V. Roeloffs, and M. Lustig, "Untrained modified deep decoder for joint denoising and parallel imaging reconstruction," in *Proceedings of the 28th Annual Meeting of the ISMRM*, 2020, p. 3585.
- [58] Z. Ke, Y. Zhu, J. Cheng, L. Ying, X. Liu, H. Zheng, and D. Liang, "Assessment of the generalization of learned unsupervised deep learning method," in *Proceedings of the 28th Annual Meeting of the ISMRM*, 2020, p. 3630.
- [59] Q. Zou, A. H. Ahmed, P. Nagpal, S. Kruger, and M. Jacob, "Deep generative STORM model for dynamic imaging," *arXiv preprint arXiv:2101.12366*, 2021.
- [60] D. Narnhofer, K. Hammernik, F. Knoll, and T. Pock, "Inverse GANs for accelerated MRI reconstruction," in *Proceedings of the SPIE*, vol. 11138, 2019, pp. 381 – 392.

- [61] K. C. Tezcan, C. F. Baumgartner, R. Luechinger, K. P. Pruessmann, and E. Konukoglu, "MR image reconstruction using deep density priors," *IEEE Transactions on Medical Imaging*, vol. 38, no. 7, pp. 1633–1642, 2019.
- [62] A. Gabbay and Y. Hoshen, "Style generator inversion for image enhancement and animation," *arXiv preprint arXiv:1906.11880*, 2019.
- [63] Y. Korkmaz, S. U. Dar, M. Yurt, M. Ozbey, and T. Çukur, "Zero-shot learning for unsupervised reconstruction of accelerated mri acquisitions," in *Proceedings of the 29th Annual Meeting of the ISMRM*, 2021.
- [64] T. Karras, S. Laine, and T. Aila, "A style-based generator architecture for generative adversarial networks," in *Proceedings of the IEEE/CVF Conference on Computer Vision and Pattern Recognition (CVPR)*, 2019, pp. 4401–4410.
- [65] T. Karras, S. Laine, M. Aittala, J. Hellsten, J. Lehtinen, and T. Aila, "Analyzing and improving the image quality of StyleGAN," in *Proceedings of the IEEE/CVF Conference on Computer Vision and Pattern Recognition (CVPR)*, 2020, pp. 8107–8116.
- [66] D. A. Hudson and C. L. Zitnick, "Generative adversarial transformers," *arXiv preprint arXiv:2103.01209*, 2021.
- [67] H. Zhang, I. Goodfellow, D. Metaxas, and A. Odena, "Self-attention generative adversarial networks," in *Proceedings of the 36th International Conference on Machine Learning*, 2019, pp. 7354–7363.
- [68] D. Ulyanov, A. Vedaldi, and V. Lempitsky, "Deep image prior," in *Proceedings of the IEEE Conference on Computer Vision and Pattern Recognition (CVPR)*, 2018, pp. 9446–9454.
- [69] M. Akçakaya, S. Moeller, S. Weingärtner, and K. Uğurbil, "Scan-specific robust artificial-neural-networks for k-space interpolation (RAKI) reconstruction: Database-free deep learning for fast imaging," *Magnetic Resonance in Medicine*, vol. 81, no. 1, pp. 439–453, 2019.
- [70] S. A. H. Hosseini, C. Zhang, S. Weingärtner, S. Moeller, M. Stuber, K. Ugurbil, and M. Akçakaya, "Accelerated coronary MRI with sRAKI: A database-free self-consistent neural network k-space reconstruction for arbitrary undersampling," *PLOS ONE*, vol. 15, no. 2, pp. 1–13, 2020.
- [71] T. H. Kim, P. Garg, and J. P. Haldar, "LORAKI: Autocalibrated recurrent neural networks for autoregressive MRI reconstruction in k-space," *arXiv preprint arXiv:1904.09390*, 2019.
- [72] Y. Arefeen, O. Beker, H. Yu, E. Adalsteinsson, and B. Bilgic, "Scan-specific, parameter-free artifact reduction in k-space (SPARK)," *arXiv preprint arXiv:2104.01188*, 2021.
- [73] J. Zhu, Y. Shen, D. Zhao, and B. Zhou, "In-domain GAN inversion for real image editing," in *Proceedings of European Conference on Computer Vision (ECCV)*, 2020, pp. 592–608.
- [74] W. Xia, Y. Zhang, Y. Yang, J.-H. Xue, B. Zhou, and M.-H. Yang, "GAN inversion: A survey," *arXiv preprint arXiv:2101.05278*, 2021.
- [75] R. Abdal, Y. Qin, and P. Wonka, "Image2stylegan: How to embed images into the stylegan latent space?" in *Proceedings of the IEEE/CVF International Conference on Computer Vision*, 2019, pp. 4432–4441.
- [76] M. Uecker, P. Lai, M. J. Murphy, P. Virtue, M. Elad, J. M. Pauly, S. S. Vasanawala, and M. Lustig, "ESPIRiT-an eigenvalue approach to autocalibrating parallel MRI: Where SENSE meets GRAPPA," *Magnetic Resonance in Medicine*, vol. 71, no. 3, pp. 990–1001, 2014.
- [77] F. Knoll, J. Zbontar, A. Sriram, M. J. Muckley, M. Bruno, A. Defazio, M. Parente, K. J. Geras, J. Katsnelson, H. Chandarana, Z. Zhang, M. Drodzdzal, A. Romero, M. Rabbat, P. Vincent, J. Pinkerton, D. Wang, N. Yakubova, E. Owens, C. L. Zitnick, M. P. Recht, D. K. Sodickson, and Y. W. Lui, "fastMRI: A publicly available raw k-space and DICOM dataset of knee images for accelerated MR image reconstruction using machine learning," *Radiology: Artificial Intelligence*, vol. 2, no. 1, p. e190007, 2020.
- [78] T. Zhang, J. M. Pauly, S. S. Vasanawala, and M. Lustig, "Coil compression for accelerated imaging with Cartesian sampling," *Magnetic Resonance in Medicine*, vol. 69, no. 2, pp. 571–82, 2013.
- [79] R. Child, S. Gray, A. Radford, and I. Sutskever, "Generating long sequences with sparse transformers," *arXiv preprint arXiv:1904.10509*, 2019.
- [80] P. Esser, R. Rombach, and B. Ommer, "Taming transformers for high-resolution image synthesis," *arXiv preprint arXiv:2012.09841*, 2020.
- [81] Y. Wu, Y. Ma, J. Liu, J. Du, and L. Xing, "Self-attention convolutional neural network for improved MR image reconstruction," *Information Sciences*, vol. 490, pp. 317–328, 2019.
- [82] H. Lan, A. W. Toga, and F. Sepehrband, "SC-GAN: 3D self-attention conditional GAN with spectral normalization for multi-modal neuroimaging synthesis," *bioRxiv preprint 2020.06.09.143297*, 2020.
- [83] O. Oktay, J. Schlemper, L. L. Folgoc, M. Lee, M. Heinrich, K. Misawa, K. Mori, S. McDonagh, N. Y. Hammerla, B. Kainz, B. Glocker, and D. Rueckert, "Attention U-Net: Learning where to look for the pancreas," *arXiv preprint arXiv:1804.03999*, 2018.
- [84] Z. Yuan, M. Jiang, Y. Wang, B. Wei, Y. Li, P. Wang, W. Menpes-Smith, Z. Niu, and G. Yang, "SARA-GAN: Self-attention and relative average discriminator based generative adversarial networks for fast compressed sensing MRI reconstruction," *Frontiers in Neuroinformatics*, vol. 14, p. 58, 2020.
- [85] J. Chen, Y. Lu, Q. Yu, X. Luo, E. Adeli, Y. Wang, L. Lu, A. L. Yuille, and Y. Zhou, "TransUNet: Transformers make strong encoders for medical image segmentation," *arXiv preprint arXiv:2102.04306*, 2021.

SUPPLEMENTARY MATERIALS

A. Supplementary Text

1) Architecture Details:

a) Synthesizer: Resolution 4x4: Input (Constant) \rightarrow Modulated Convolution \rightarrow Cross-Attention + Noise \rightarrow Output
 Resolution 8x8: Input \rightarrow Upsample \rightarrow Cross-Attention Transformer Block + Upsample(Input) \rightarrow Output
 Resolution 16x16: Input \rightarrow Upsample \rightarrow Cross-Attention Transformer Block + Upsample(Input) \rightarrow Output
 Resolution 32x32: Input \rightarrow Upsample \rightarrow Cross-Attention Transformer Block + Upsample(Input) \rightarrow Output
 Resolution 64x64: Input \rightarrow Upsample \rightarrow Cross-Attention Transformer Block + Upsample(Input) \rightarrow Output
 Resolution 128x128: Input \rightarrow Upsample \rightarrow Cross-Attention Transformer Block + Upsample(Input) \rightarrow Output
 Resolution 256x256: Input \rightarrow Upsample \rightarrow Modulated Convolution \rightarrow Output

Cross-attention Transformer Block:

Input \rightarrow Cross-Attention + Noise \rightarrow Modulated Convolution \rightarrow Cross-Attention + Noise \rightarrow Output

b) Mapper: Input \rightarrow Self-Attention Block x4 \rightarrow Dense Layer \rightarrow Output

Self-Attention Block: Input \rightarrow Self-Attention \rightarrow Dense Layer \rightarrow Dense Layer + Input \rightarrow Output

c) Discriminator: Resolution 256x256: Input \rightarrow Convolution \rightarrow Downsample+ Downsample (Input) \rightarrow Output

Resolution 128x128: Input \rightarrow Convolution \rightarrow Downsample+ Downsample (Input) \rightarrow Output

Resolution 64x64: Input \rightarrow Convolution \rightarrow Downsample+ Downsample (Input) \rightarrow Output

Resolution 32x32: Input \rightarrow Convolution \rightarrow Downsample+ Downsample (Input) \rightarrow Output

Resolution 16x16: Input \rightarrow Convolution \rightarrow Downsample+ Downsample (Input) \rightarrow Output

Resolution 8x8: Input \rightarrow Convolution \rightarrow Downsample+ Downsample (Input) \rightarrow Output

Resolution 4x4: Input \rightarrow Convolution \rightarrow Flatten \rightarrow Dense \rightarrow Dense \rightarrow Output

2) Network Details and Hyperparameter Selections:

a) GAN_{sup} : Generator and discriminator networks were trained simultaneously for 100 epochs. Adam optimizer was used with parameters $\beta_1 = 0.5$ and $\beta_2 = 0.999$. For both generator and discriminator, learning rate was constant for the first 50 epochs and linearly decayed to 0 in the last 50 epochs. Weightings for (Pixel-wise, Perceptual, Adversarial) losses were set to (100,100,1). Dropout regularization was used with a rate of 0.5.

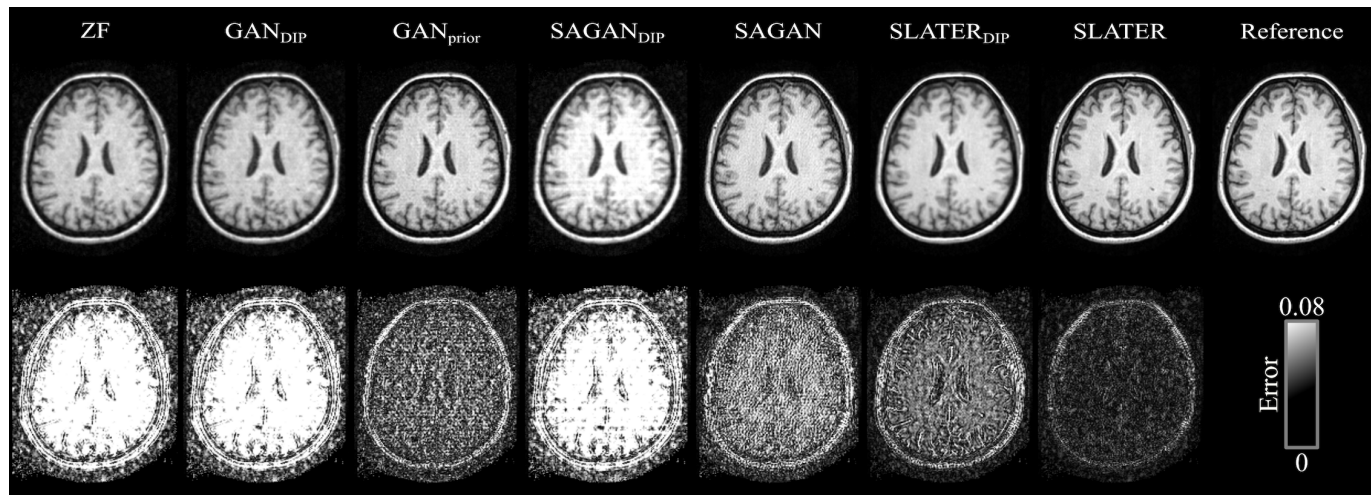
b) $SSDU$: Adam optimizer with parameters $\beta_1 = 0.5$ and $\beta_2 = 0.999$ was used to train the network for 100 epochs. Learning rate was constant for the first 50 epochs and linearly decayed to 0 in the last 50 epochs. Dropout regularization was used with a rate of 0.5.

c) GAN_{prior} : The synthesis network in GAN_{prior} was trained to minimize the same loss as in Eq. 10 with an additional path length regularization parameter adopted from [65]. Discriminator and Mapper networks were trained to minimize the losses in Eq. 14 and Eq. 13 respectively. During

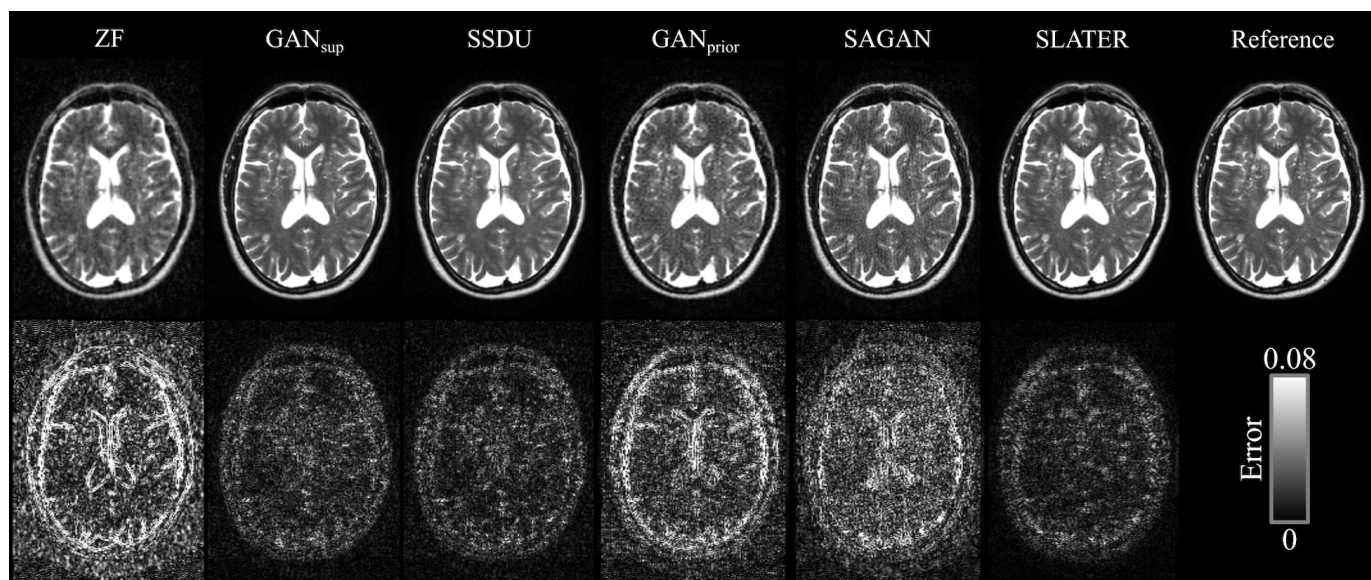
training, Adam optimizer with parameters $\beta_1 = 0$ and $\beta_2 = 0.99$ was used. During inference the regularization parameters in Eq. 15 were chosen as $\lambda_1 = 1, \lambda_2 = 0$.

d) $SAGAN$: Training and inference procedures were identical to SLATER as explained in Methods-A, except that network weights were fixed at their pretrained values as optimizing the weights was observed to yield suboptimal performance.

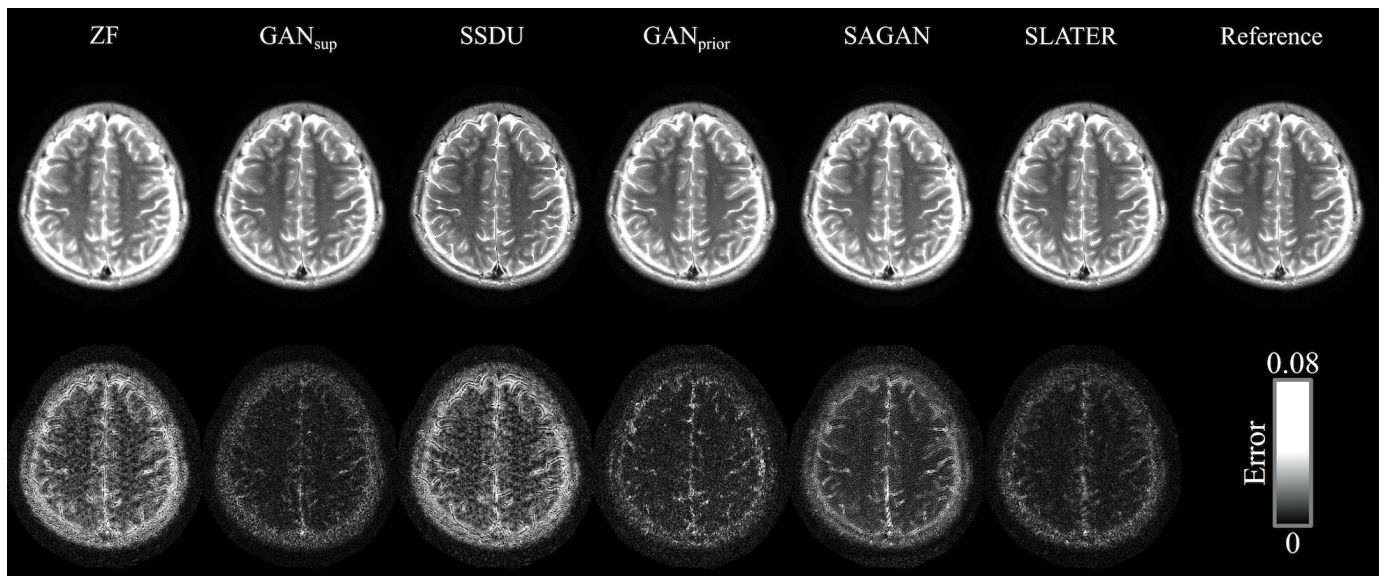
B. Supplementary Figures



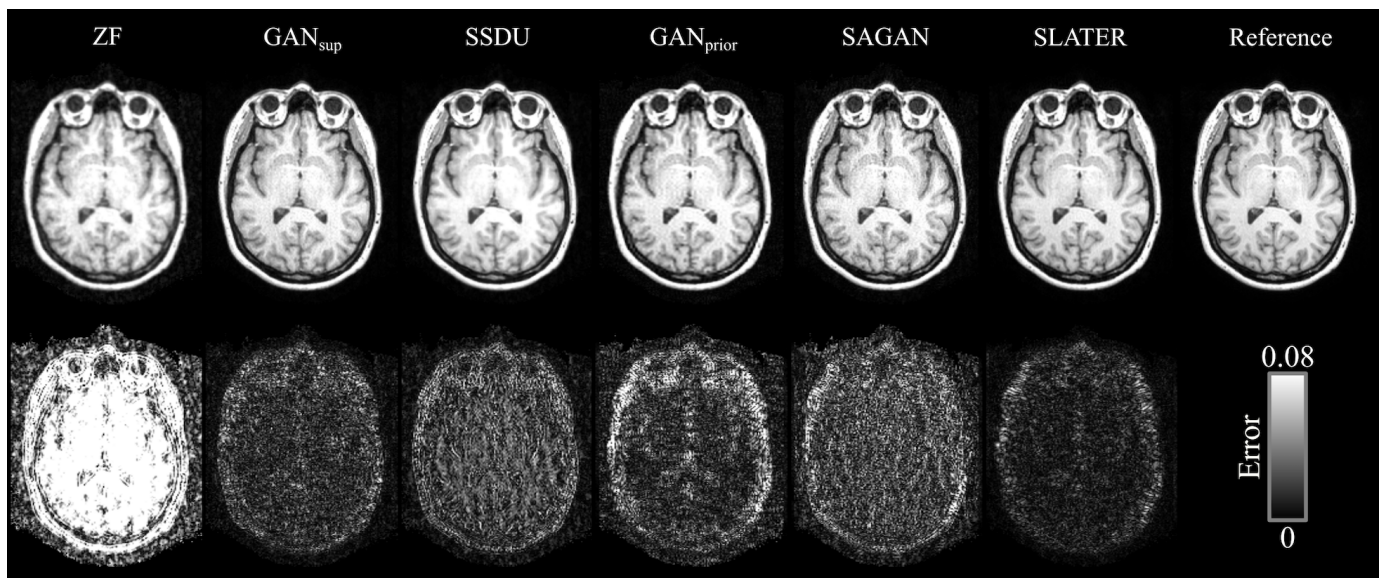
Supp. Fig. 1: Reconstructions of a representative T_1 -weighted acquisition at $R=4$ are shown for the Fourier method (ZF), DIP methods (GAN_{DIP} , $SAGAN_{DIP}$, $SLATER_{DIP}$) and zero-shot reconstructions (GAN_{prior} , SAGAN, SLATER) along with the reference image. Corresponding error maps are underneath the images for each method.



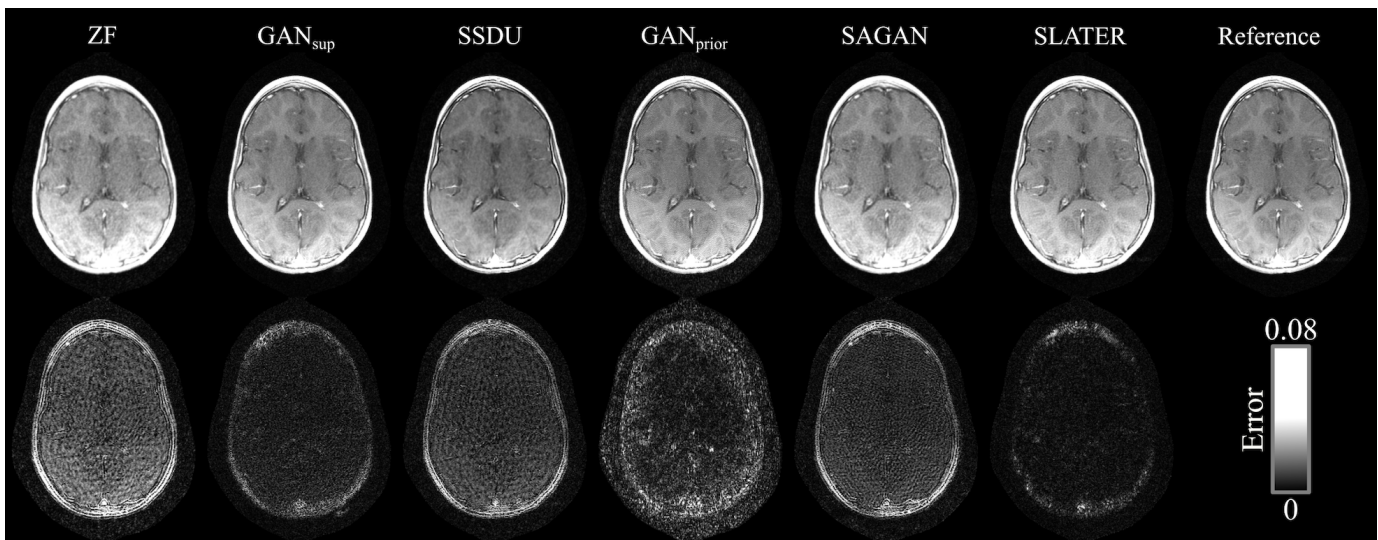
Supp. Fig. 2: Within-domain reconstructions of a T_2 -weighted acquisition in the IXI dataset at $R=4$. Results are shown for ZF, GAN_{sup} , SSDU, GAN_{prior} , SAGAN and SLATER along with the reference image. Corresponding error maps are underneath the images for each method.



Supp. Fig. 3: Within-domain reconstructions of a T_2 -weighted acquisition in the fastMRI dataset at $R=4$. Results are shown for ZF, GAN_{sup} , SSDU, GAN_{prior} , SAGAN and SLATER along with the reference image. Corresponding error maps are underneath the images for each method.



Supp. Fig. 4: Across-domain reconstructions of a T_1 -weighted acquisition in the IXI dataset at $R=4$. Results are shown for ZF, GAN_{sup} , SSDU, GAN_{prior} , SAGAN and SLATER along with the reference image. Corresponding error maps are underneath the images for each method.



Supp. Fig. 5: Across-domain reconstructions of a T_1 -weighted acquisition in the fastMRI dataset at $R=4$. Results are shown for ZF, GAN_{sup} , SSDU, GAN_{prior} , SAGAN and SLATER along with the reference image. Corresponding error maps are underneath the images for each method.